Materials Advances

ROYAL SOCIETY OF CHEMISTRY

PAPER

View Article Online
View Journal | View Issue



Cite this: *Mater. Adv.*, 2025, **6**, 8078

# Investigating the impact of heating rates on hydrothermal conversion of heat-treated kaolin into Linde-type LTA zeolite for water vapor sorption

Cyrille Ghislain Fotsop, Alexandra Lieb and Franziska Scheffler*

This study focuses on the impact of heating rates on the hydrothermal conversion of heat-treated kaolin into zeolite LTA. Kaolin was heat-treated at three different heating rates: 5, 20, and 40 K $min^{-1}$. The synthesized zeolites were characterized using X-ray diffraction (XRD), Raman spectroscopy, $^{27}Al$ and $^{29}Si$ solid-state magic angle spinning (MAS)-nuclear magnetic resonance (NMR), field emission scanning electron microscopy (FE-SEM)/energy dispersive X-ray spectroscopy (EDX), $N_2$ sorption, Micromeritics AutoPore IV mercury porosimeter, and Fourier transform infrared spectroscopy (FTIR) techniques. XRD patterns showed relative crystallinities of 85.5%, 83.2%, and 81.0% for zeolite A synthesized from metakaolin samples MK-(5), MK-(20), and MK-(40), respectively. Samples synthesized from metakaolin at higher heating rates (20 and 40 K $min^{-1}$) also contained sodalite and quartz. SEM images revealed cubic particles and spine shaped crystals in all zeolite samples. The BET surface areas were 23, 29, and 31 $m^2$ $g^{-1}$ for the zeolite samples obtained using MK-(5), MK-(20), and MK-(40), respectively. Metakaolin was suitable for preparing zeolite A, and the water vapor adsorption capacity of the synthetic zeolite followed this order: Zeo-4A-MK-40 > Zeo-4A-MK-20 > Zeo-4A-MK-5, with maximum adsorption capacities were 15.3, 14.6, and 9.1 mg $g^{-1}$, respectively. GAB isotherm models were found to be more suitable for adjusting the experimental data, with $R^2$ values above 0.9.

Received 25th June 2025,
Accepted 30th September 2025

DOI: 10.1039/d5ma00678c

rsc.li/materials-advances



## 1. Introduction

Moisture fluctuation and mould continue to appear in drying and industrial synthesis processes.[1] Humidity removal reduces the damaging effects and the energy requirement during the gas separation and extraction process.[2] Drying and adsorption are among the most widely used techniques for the elimination of moisture; however, drying is more energy-consuming. Adsorption, one of the most reliable and least expensive techniques for the removal of moisture, involves the use of suitable adsorbents that provide the most effective adsorption performance and the optimum interaction between adsorbent and adsorbate.[3] Silica gels,[4] metal–organic frameworks,[5] and X-type zeolites,[6] have proved to be interesting for moisture removal. Most of the above-mentioned adsorbents offer high performance adsorption, although their synthesis remains a challenge for the scientific project, as the synthetic reagents required remain costly. Kaolin, which has an uncharged 1 : 1 di-octahedral layered structure, in which each layer of silica tetrahedral is connected to layers of alumina tetrahedral with pseudo-hexagonal symmetry, with a Si/Al ratio close to that of 4A zeolites,[7] is one of the main natural minerals available in Cameroon and provides a primary and alternative supply as a precursor for the synthesis of zeolites. Type A zeolite is one of the most suitable adsorbents for moisture removal and offers a strong affinity with the water molecules, $Na^+$ ions and oxygen atoms within the zeolite structure. Linde-type LTA zeolites are homogeneous crystalline microporous aluminosilicates and alkali metal hydrates.[8] With a tetrahedral structure of $[SiO_4]^{4-}$ and $[AlO4]^{5-}$, their compilation allows them to have an open structure with a network of negative charges balanced by $Na^+$ ions.[9] Type 4A zeolite, with a Si/Al ratio close to 1, is one of the most studied varieties, due to its high ion exchange capacity in solution, its high diffusion capacity, and its high thermal and mechanical resistances, for various applications in adsorption and water treatment.[10]

The synthesis of zeolites using kaolin as a silica and aluminum supplier requires kaolin in an amorphous form such as metakaolin. Metakaolin is obtained by the thermal treatment of kaolin at high temperatures, about 900 °C.[3,11] Heat treatment promotes the alteration of aluminum ions through the deformation of the Si–O lattice and the formation of a new

*Otto-von-Guericke-University Magdeburg, Chemical Institute, Chair for Industrial Chemistry, Universitätsplatz 2, 39106 Magdeburg, Germany.*
*E-mail: franziska.scheffler@ovgu.de*

quadruple coordination between Si–O and Al–O, leading to a more amorphous and easily modulated phase.[12] Previous work has shown that direct reactions between kaolinite and NaOH produce mainly hydroxysodalite as the final product,[13] while the reactions between metakaolin and NaOH produce mainly zeolite Na–A as the final product.[14] Several researchers have investigated the synthesis of zeolites using metakaolin obtained at a single heating rate, for example, Ayele *et al.* (2016) reported the synthesis of Na–A zeolite with a relative crystallinity of around 90% using ethiopian kaolin. This study was based on the optimization of parameters involved in the synthesis; such as aging time, crystallization temperature, time and NaOH concentration.[15]

Cristóbal *et al.* (2010), reported on the synthesis of zeolite Na–A, using kaolin samples with different contents, they show that a kaolin sample with 7% kaolinite and 89% quartz in the content, is unsuitable for the synthesis of zeolite A, due to the high quartz content, while for a kaolin sample containing 5% of quartz, 47% of $SiO_2$ and 39% of $Al_2O_3$, promotes the production of zeolite A when it is treated by mechanical activation with 5 M sodium hydroxide for 5 h at 90 °C.[14] Belviso *et al.* (2015) report the synthesis of zeolites with an average particle size of 1 μm using the alkaline fusion method with a NaOH/kaolin ratio of 1.2. They deduce that the variation in zeolite crystal size depends on the steric stabilization of the nuclei and high NaOH supersaturation.[11] Similarly, Alkan *et al.* (2005) reported on the alkaline fusion process during the synthesis of zeolite Na–A from Turkish kaolin. In this study, they evaluated the influence of the NaOH/kaolin molar ratio and NaOH concentration, followed by hydrothermal treatment for 24 h at 105 °C. It was found that a high NaOH/kaolin ratio led to the formation of Type A phases zeolite, while high values of sodium hydroxyl concentration induced the formation of hydroxysodalite phases.[16] To our knowledge, the impact of heating rate during the hydrothermal conversion of kaolin to metakaolin and the subsequent use of the derived products for zeolite synthesis remain little explored.

This work investigates the impact of heating rate during the hydrothermal conversion of metakaolin to zeolite A, derived from the thermal conversion of cameroonian kaolin. The present work is a continuation of our previous work on the pyrolysis kinetics of cameroonian kaolin and the understanding of deyhdroxylation mechanisms on the influence of zeolite microstructure. It is also in line with our work on the development of adsorbents from Cameroonian kaolin, as well as on the valorization of basic clay materials. Beyond the synthesis process, the derived zeolites were tested for water vapor adsorption, followed by the experimental data modeling using non-linear isothermal models of Langmuir, Freundlich, Sips and Guggenheim, Anderson and De Boer (GAB) relying on the correlation coefficient ($R^2$) to describe the interactions and mechanisms between adsorbate and adsorbent. The choice of isotherm depends on the quality of the available information needed to explain the observed phenomena. The Langmuir isotherm assumes adsorption occurs on a homogeneous monolayer due to the gradual filling of nonreactive adsorption sites on the adsorbent's surface. In contrast, the Freundlich and Sips isotherms assume that adsorption energy decreases proportionally to the decrease in adsorption sites on the adsorbent surface. The GAB model is based on assumptions of infinite single-layer and multilayer adsorption at high and low pressures, as well as heterogeneous surfaces with energy heterogeneity. This occurs within the typical operating relative humidity range, where single-layer and multilayer adsorption occurs due to capillary condensation.

One of the main innovations of this work lies in the methodology adopted and the choice of raw material, the use of kaolin as a precursor providing a cost-effective and sustainable approach for the synthesis of zeolites. Metakaolin-derived zeolite samples obtained at 5, 20 and 40 K $min^{-1}$ were characterized using several physico-chemical techniques, including X-ray diffraction, Fourier transform infrared and Raman spectroscopy, $N_2$ sorption, field emission scanning electron microscopy and solid-state magic angle spinning nuclear magnetic resonance spectroscopy.

## 2. Materials and experimental procedure

### 2.1. Materials

Kaolin collected in the West Region of Cameroon (Fig. S1 in the SI) was used in the present study. The materials for the zeolite synthesis, sodium hydroxide (NaOH, puriss p.a.) and sodium aluminum ($NaAlO_2$, technical grade), were purchased from Sigma-Aldrich (St. Louis, USA) and Honeywell Fluka (Fisher Scientific GmbH, Schwerte, Germany), respectively, and used without further purification. For the determination of the crystallinity of zeolite 4A a standard sample stocked at the group of industrial chemistry at Otto-von-Guericke-University, Magdeburg, was used. For comparison with the diffraction patterns of the derived zeolite samples a commercial zeolite 4A, Köstrolith® 4AK (CWK, Bad Köstritz, Germany) was used.

### 2.2. Experimental procedure

**2.2.1 Thermal treatment of cameroonian kaolin.** For the thermogravimetric measurements, 1.5 g of kaolin was used. Thermogravimetric analyses were carried out using three heating rates, namely 5, 20 and 40 K $min^{-1}$, over a temperature range from 25 to 1100 °C. The metakaolin samples obtained were labelled MK ($x$), where $x$ represents the heating rate.

**2.2.2 Zeolite synthesis.** All three zeolite samples were obtained by hydrothermal synthesis as follows: 1 g of metakaolin obtained from each of the three TGA experiments (heating rates: 5, 20 and 40 K $min^{-1}$) was mixed with 25 mL of 4M NaOH solution under stirring at 600 rpm at 60 °C for 2 h. Then 0.2 g of sodium aluminum $NaAlO_2$ was added to adjust the Si/Al ratio to 1. The mixture was stirred at 60 °C for 4 h. Then the gel mixture was transferred into a 60 mL Teflon-lined autoclave and placed in an oven for the crystallization step at 90 °C for 5 h. After cooling to room temperature, the mixture was filtered and washed several times with distilled water until the pH was

decreased to about 8. The resulting product was dried overnight at 100 °C in an oven under air. The resulting zeolite samples were designated Zeo-4A-MK-*x*, where *x* represents the heating rate of the TGA experiment, which delivered the metakaolin starting material.

**2.2.3 Dynamic vapor sorption measurement.** Water vapor adsorption was performed gravimetrically with the Dynamic Vapour Sorption (DVS) instrument using an automatic vapor adsorption analyzer (DVS Vacuum, Surface Measurement Systems Ltd, England), in a relative humidity range of (0–98%) at 20 °C. Zeolite samples were activated at 200 °C for 4 h to remove all adsorbed water molecules, 15 mg of each sample was placed in the microbalance of the DVS instrument, then the samples were exposed to the desired relative humidity; the mass change was recorded using an ultra-sensitive balance with an accuracy of 0.1 μg.

### 2.3. Characterization techniques

The structural identity of all samples was determined using X-ray diffraction (XRD) using an Empyrean powder diffractometer (PANanalytical, Almelo, The Netherlands) equipped with a Cu-tube (wavelengths $K_{\alpha1}$ = 1.540598 Å and $K_{\alpha2}$ = 1.544426 Å) operating at 40 mA and 40 kV. All samples were scanned from 4–90°2$\theta$. The morphology and microstructure of all samples was recorded using a FEI SEM XL30 field emission scanning electron microscope (FEI, Hillsboro, USA) equipped with an energy dispersive X-ray spectrometer at an acceleration voltage of 20 kV. Fourier transform infrared spectroscopy (FT-IR) data was recorded using a Nicolet iS50 IR spectrometer (Thermo Scientific, Schwerte, Germany) in the 4000–200 $cm^{-1}$ wavenumber range. Thermo gravimetric analysis (TGA) and differential thermal analysis (DTA) were performed using a LECO TGA-701 (LECO, St. Joseph, USA) for large samples (approx. 1.5 g) and a Netzsch STA 449C Jupiter (Netzsch, Selb, Germany) thermogravimetric analyzer. Raman analysis was performed with a Lab-RAM HR evolution (Horiba, Oberursel, Germany) using a monochromatic laser with a wavelength of 532 nm. Solid state $^{29}Si$ and $^{27}Al$ MAS NMR analyses were performed using a Bruker AVANCE II 400WB spectrometer (Bruker, Billerica, USA) with a frequency of 12 kHz. $N_2$ sorption isotherms were recorded using a Micromeritics 3Flex instrument (Micromeritics, Norcross, USA). For the sorption analysis, all samples were first heated to 250 °C under vacuum and then activated at 350 °C for 5 h under vacuum and the freespace was determined after each measurement with reactivated samples. The pore size distribution was measured using an AutoPore IV mercury intrusion porosimeter (Micromeritics, USA).

## 3. Results and discussion

### 3.1. SEM analysis of cameroonian kaolin (starting material) and its products MK-(5), MK-(20) and MK-(40) from thermal treatment

FE-SEM images of kaolin and metakaolin (MK-(5), MK-(20) and MK-(40)) are shown in Fig. 1. The kaolin image (Fig. 1a), shows a morphology with a stack of parallel tetrahedral and octahedral layers of the kaolinite present in the kaolin, displaying a typical kaolinite morphology.[17] However, a few discontinuities with parallel geometries and variable thicknesses are also observable. These geometries of variable sizes can be explained by the presence of quartz and illite in the kaolin. Metakaolin MK-(5) (Fig. 1b), which has a more disordered morphology and

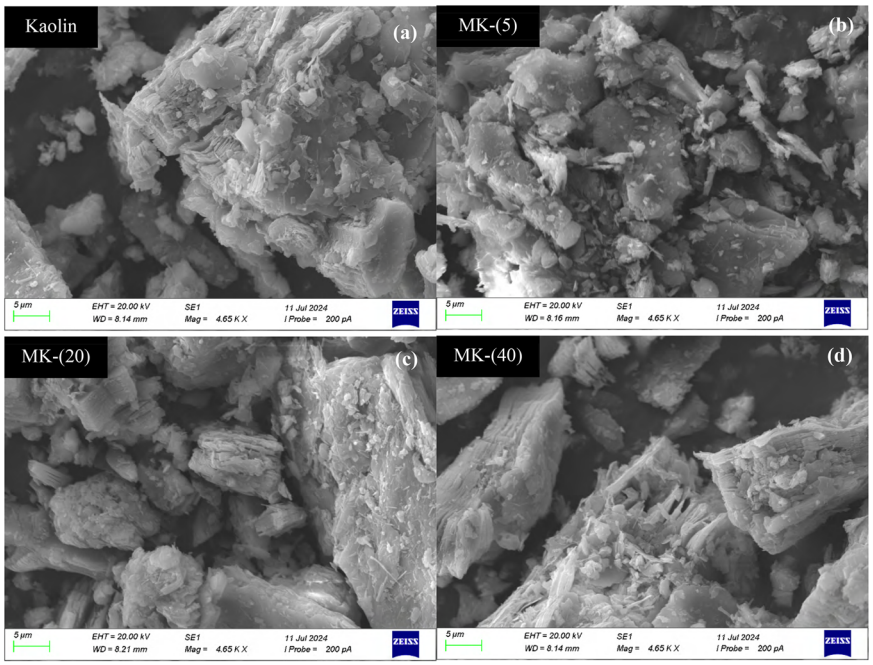


Fig. 1 SEM images of kaolin (a) and metakaolin samples MK-(5) (b), MK-(20) (c) and MK-(40) (d), achieved by TG measurements using 5, 20 and 40 K $min^{-1}$ as heating rate.

 

is altered into parallel layers, is comparable to kaolin (Fig. 1a), in which the tetrahedral stacking layers have been destroyed by heat treatment. Heat treatment enhanced the destruction of the kaolin crystalline phase into a more disordered amorphous phase. However, MK-(20) and MK-(40) (Fig. 1c and d), present particles with morphologies having a more visible kaolin-like stacking of parallel layers.[18] Furthermore, the delamination of layers that occurred at lower heating rates could be explained by the fact that low heating rates provide to the system more time and energy to reach the final equilibrium temperature, in order to enhance the dehydration and dehydroxylation of Si–OH and Al–OH bonds from the outside to the kaolin core, comparable to 20 and 40 K $min^{-1}$ heating rates.[19,20] Irfan Khan *et al.* (2017) reported that the dehydroxylation of kaolin starts on the Al–OH bonds bound to the outer edges of the kaolin and progresses towards the inner edges. These observations show that low heating rates would promote the dehydroxylation of kaolin layers and their transformation into a more disordered amorphous phase.[21]

### 3.2. X-ray diffraction, FT-IR, Raman and TGA/DTG analyses of kaolin and its products MK-(5), MK-(20) and MK-(40) from thermal treatment

XRD patterns of kaolin and its calcination products are shown in Fig. 2a. The diffractogram shows that kaolin is made up of illite, quartz and kaolinite according to standard data from the Joint Committee on Powder Diffraction Standards (JCPDS).[22] This suggests that the by-products of heat treatment may be suitable for the preparation of zeolites.[7] The metakaolin (MK-(5), MK-(20) and MK-(40)) obtained after heat treatment shows the lack of the intense peaks characteristic of illite and kaolinite. Heat treatment leads to the transformation of the crystalline and ordered structure of kaolin into a more reactive and amorphous phase, through the elimination of hydroxyl groups and the destruction of the tetrahedral aluminum and silica layers present in the kaolin.[23] The cascade plot of the diffraction patterns of the cameroonian kaolin and its derived metakaolin samples (MK-(5), MK-(20), and MK-(40)) clearly shows the amorphous background representing the metakaolin (Fig. S2). In addition, the metakaolin obtained is predominantly quartz with reflection peaks aligned with those of kaolin. Metakaolin containing sodium silicate and aluminum silicate is the most reactive phase during the zeolitization process.[7] However, the metakaolin pattern are almost identical, due to the presence of the strong reflections quartz confined within the kaolin. The associated SEM analyses (Section 3.1), enable us to better appreciate the effect of heating rate during heat treatment. These observations show that high heating rates promote the partial transformation of the crystalline and ordered structure of kaolin into metakaolin.[7,18]

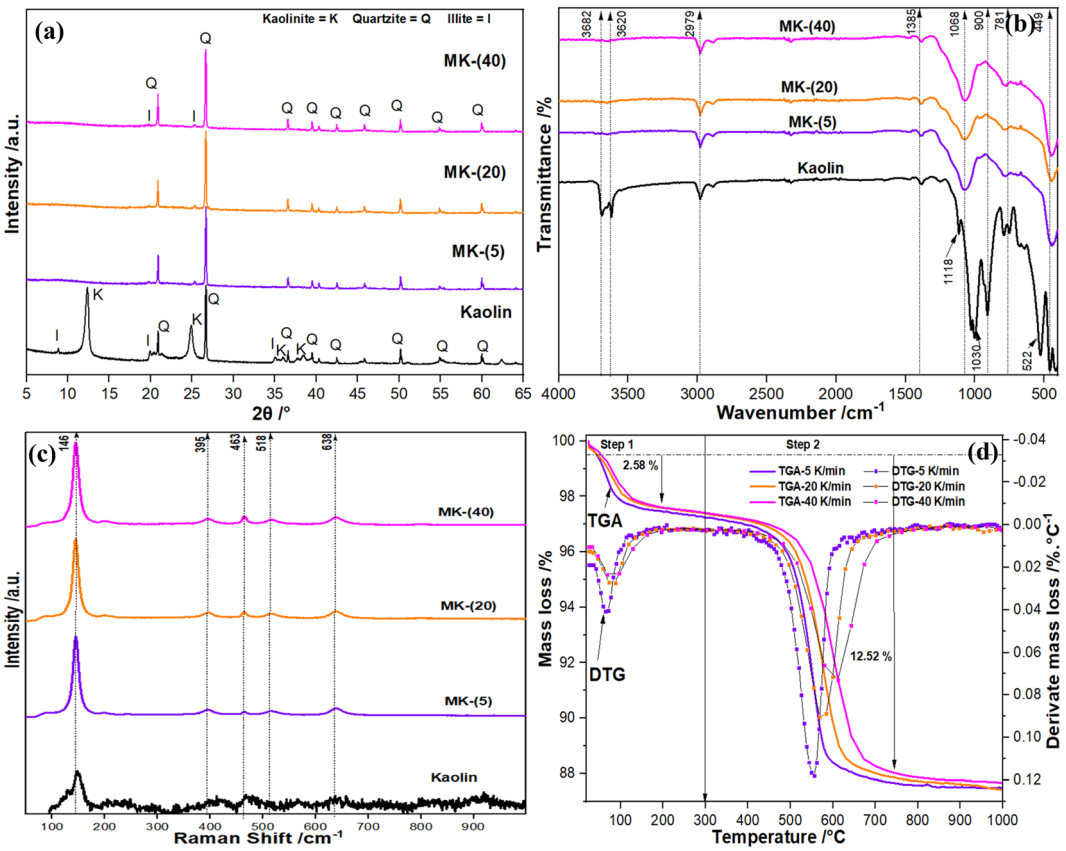


Fig. 2 XRD patterns (a), FT-IR (b), Raman spectra (c) and TGA/DTG curve (d) of cameroonian kaolin (starting material) collected using a LECO TGA-701 (LECO, St. Joseph, USA) with 5, 20 and 40 K $min^{-1}$ heating rate and metakaolin samples MK-(5), MK-(20) and MK-(40). The kaolin pattern shows the presence of kaolinite (K), illite (I), quartz (Q) and an amorphous phase. The measurements were performed using a PANalytical Empyrean diffractometer with Cu $K_{\alpha 1+\alpha 2}$ radiation.

Fig. 2b shows the FT-IR spectra of kaolin and its activated samples at different heating rates. The O-H stretching vibration bands of the interlayer hydroxyl group present in kaolin are those located at 3682 $cm^{-1}$.[18] The broad band at 3620 $cm^{-1}$ is attributable to the O-H bonds of bound water molecules. The Si–OH elongation bands are attributable to those located at 2979–2900 $cm^{-1}$. The asymmetric stretching vibration bands of the Al–O and Si–O bonds are those appearing at 1385 and 1030 $cm^{-1}$.[24,25] Bands at 990, 781, 522 $cm^{-1}$ are attributable to Al–O, Si–O–Si and Al–O–Si bonds.[7,26] After heat treatment, metakaolin (MK-(5), MK-(20) and MK-(40)) misses the strong bands at 3690 and 3620 $cm^{-1}$, indicating the formation of metakaolin. The formation of metakaolin is also confirmed by the presence of new vibrational bands with chemical shifts at 1068 and 449 $cm^{-1}$, are attributable to the Al–O–Si and Si–O-Al bonds of sodium aluminum silicate in the amorphous phase of metakaolin, comparable to kaolin.[26,27]

Fig. 2c presents the Raman spectra of cameroonian kaolin and the metakaolin samples MK-(5), MK-(20) and MK-(40), achieved at different heating rates. The low intensity of the peaks for the kaolin sample could be due to the presence of OH groups in Si octahedra and alumina tetrahedra, which tend to absorb the excitation laser and produce florescence that may be interfering with the Raman diffusion signal reflected by the kaolin. However, five major peaks at 146, 396, 463, 518 and 638 $cm^{-1}$ were observed in all samples obtained after heat treatment. The peaks at 146 $cm^{-1}$ are attributable to the intra-tetrahedral vibrational modes of the polymerized tetrahedron ($SiO_4$) present in crystalline quartz. Those at 396 $cm^{-1}$ and 463 $cm^{-1}$ are assimilated to the bending modes of Si–O-Al and Al–O–Si, respectively, of aluminum and sodium silicate in amorphous metakaolin,[28] while peaks at 518 $cm^{-1}$ are attributable to the bending modes of Si–O–Si. The peaks at 638 $cm^{-1}$ correspond to the symmetrical stretching mode of the T–O bands (T = Al or Si).[29] Similar findings were observed by Mahrous *et al.* (2024), on metakaolin used for the preparation of geopolymers. Furthermore, an increase of the Raman signal intensity and of the peak half-maximum width (FWHM) are observed with the increase of the heating rate, as can be seen for the peaks at 463 $cm^{-1}$ and 638 $cm^{-1}$. The increase in FWHM shows that the vibrational mode associated with these peaks becomes more disordered,[30] resulting from the changes in the bonding spacing and angles, with the increase of the heating rate. This suggests that high heating rates may be affected such factors as a changing of the local environment and an increased strength of interactions between the ($AlO_4$) and ($SiO_4$) tetrahedral molecules.[31] This shows that the product formed is a quartz-rich metakaolin, as shown by the associated XRD analyses.

Fig. 2d shows the TGA/DTG curves for kaolin treated at different heating rates (5, 20 and 40 K $min^{-1}$), the TGA curves being typical of kaolin, characterized by the presence of two endothermic peaks visible on the DTG curve appearing at different temperatures. The first, appearing between 25–180 °C, is associated with elimination of adsorbed water molecules and moisture.[32] The second peak between 300–600 °C, is attributable to the destruction of tetrahedral/octahedral sheets and dehydroxylation of the kaolinite structure. Recently, Ptáček *et al.*, 2014 reported that the kaolin dehydroxylation occurs in two steps as previously observed. This observation, shows that, during the heat treatment, the removal of hydroxyl groups from kaolin and the formation of metakaolin takes place.[32] The peak at 555 °C is attributable to the dehydroxylation followed by recombination of the silica and alumina present in the metakaolin above 900 °C. This leads to the formation of a disordered metakaolin, in which the coordination of silica in the tetrahedral sheets remains constant at 4 and that of aluminum in the octahedral sheets drops from 6 to 4.[33] This is due to the gradual oxidation of metakaolin to silicon-aluminum spinel forming the gamma-alumina structures. Above 990 °C, these spinel phases nucleate and transform into highly crystalline cristobalite and mullite.[34] The effect of heating rate on the thermal decomposition of kaolin can be seen in the shift of DTG-derived peaks in stages 1 and 2, characterized by a variation in mean temperature ($T_m$) ranging from 72.9–95.18 °C for stage 1; and 555.88–611.70 °C for stage 2. These observations are due to the small amounts of energy and time supplied to the systems to reach equilibrium temperature, as a result of the high heating rates.[35] In addition, this decrease in the overall energy of the system during heat treatment leads to a variation in diffusion energy between the outermost tetrahedral and octahedral kaolin sheets and those located towards the kaolin core. Nevertheless, the entire system contributes to metakaolin formation through strong delamination as the temperature rises to around 800 °C.[33]

The formation of reactive metakaolin is observed by the partial overlap of the TGA curves in the 800–950 °C range. Nevertheless, it is apparent that the process of dehydroxylation remains partial for samples treated at high heating rates. A mass loss of 12.52%, 12.12% and 12.01% was observed for samples treated at 5, 20 and 40 K $min^{-1}$, respectively. The possible explanation is not only the heating rate, but also the calcination time, which remains insufficient. The holding time in seconds is shown in Fig. S4. The XRD, FTIR, and SEM analyses of samples MK-5, MK-20, and MK-40 show that the high heating rates supply insufficient energy to convert kaolin to metakaolin. We previously recommended that kaolin require a minimum holding time of 10 800 seconds (three hours) after reaching a maximum heating temperature of 900 °C to obtain more reactive metakaolin, which is necessary for zeolite synthesis.[37] In addition, the innermost residual hydroxyl groups present in the kaolin structure have not had sufficient time to be eliminated. This leads to a diffusion problem at high heating rates. This observation is also confirmed by the associated SEM analyses.

## 4. Influence of the heating rate during the kaolin transformation on the subsequent synthesis of zeolite A

### 4.1. XRD analyses of Zeo-4A-MK-*x* samples achieved from the metakaolin samples MK-(5), MK-(20) and MK-(40)

Zeolite type 4A was synthesized according to the procedure described in Section 2.2.2, using metakaolin samples MK-(5),

MK-(20) and MK-(40) derived from cameroonian kaolin by thermal treatment at three different heating rates $x$ ($x$ = 5, 20 and 40 K min$^{-1}$).

All of the XRD patterns of the Zeo-4A-MK-$x$ materials (Zeo-4A-MK-5, Zeo-4A-MK-20 and Zeo-4A-MK-40) show the typical diffraction pattern of LTA zeolite type 4A (Fig. 3), identifiable by the presence of standard peaks appearing at $2\theta$ = 7.5°, 10.10°, 12.93° 16.21° and 23.01°, compared to commercial zeolite 4A (denoted as ZC).[7] Nevertheless, it should be mentioned that the kaolin samples MK-(20) and MK-(40), lead to additional sodalite reflections appearing around $2\theta$ = 14.3° and 21.02°[36] and reflections of quartz visible in the area around 28.3° and 60.23°. However, sodalite phases were observed. Based on the experimental conditions, we found that combining a short calcination time with a low crystallization temperature facilitates the formation of sodalite-rich zeolite. This is because the nucleation gel has not yet formed. The amount of energy supplied to the reaction medium is insufficient for the oligomers in the synthesis gel to transform into the crystals necessary for forming the zeolite A unit. The quantification of the crystallinity of the zeolite 4A phase present in each sample was performed by using the sum of the areas of the corresponding zeolite 4A phase compared to the corresponding area derived from sample ZC (eqn (S1)).[38] The zeolite 4A fraction of the Zeo-4A-MK-5, Zeo-4A-MK-20 and Zeo-4A-MK-40 samples showed a crystallinity of 85.50, 83.18 and 81.01%. The variance in crystallinity could be explained by the presence of sodalite and quartz in the XRD pattern of the samples Zeo-4A-MK-20 and Zeo-4A-MK-40. This presence of sodalite and quartz shows that the metakaolin samples obtained with high heating rates (20 and 40 K min$^{-1}$) have not achieved their maximum amorphous maturity. This implies that the duration of the heat treatment was not sufficient to break down the entire crystalline and ordered structure of the kaolin. Furthermore, literature findings suggest that the small amount of sodium aluminum silicate and sodium silicate formed during the thermal conversion was insufficient to enhance the crystal growth of silica and alumina oligomers formed during the gelation step. This involved the poor reconstruction of silicate-alumina subunits and the slowing down of the nucleation process. It should be noted that, although obviously low heating rates are required to improve the transformation of kaolin to metakaolin, a suitable overall reaction time is also required for the formation of the metastable and reactive phases in the kaolin samples.[39]

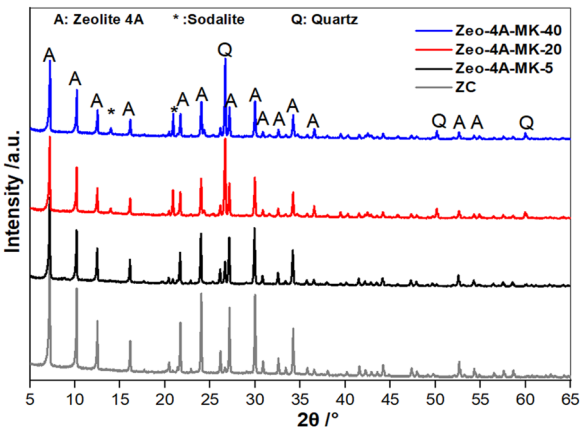


Fig. 3 Powder XRD patterns (a) and of Zeo-4A-MK-5, Zeo-4A-MK-20 and Zeo-4A-MK-40 materials and commercial zeolite NaA (ZC). The measurements were performed using a PANalytical Empyrean diffractometer with Cu $K_{\alpha1+\alpha2}$ radiation.

### 4.2. SEM, EDX and EDX-mapping analysis of Zeo-4A-MK-$x$ samples achieved from the metakaolin samples MK-(5), MK-(20) and MK-(40)

The SEM images of the three different zeolite samples Zeo-4A-MK-5, Zeo-4A-MK-20 and Zeo-4A-MK-40 show different types of morphologies (Fig. 4a–c). All samples show a fraction of almost similar crystals with cubic morphology for zeolite type 4A[40] with chamfered edge crystals[41] as well as different amounts of partially reacted layer like metakaolin and material with spine-shaped morphologies.[42] Our study showed that the matrix formed was composed of mesoporous zeolites particles and unreacted metakaolin.[43,44] At high heating rates kaolin may only partially react to metakaolin, which explains the persistent presence of sodalite and quartz in the sample after the formation of zeolite A4.[45] Indeed, the appearance of little amounts of material with spine-shaped morphologies in the SEM analysis of the sample Zeo-4A-MK-5 may indicate that the conversion of kaolin to metakaolin should even take longer than the heat treatment performed at 5 K min$^{-1}$ within our study. The EDX single spot and EDX mapping analyses (Fig. 4d and e) for the sample Zeo-4A-MK-5 showed a homogeneous distribution of the elements O, Na, Al and Si with fractions of 43.7, 20.5, 17.9 and 17.6%, respectively, present in the zeolite, which emphasizes that a zeolite of Linde type 4A has been formed.[46] EDX (Fig. S3) and EDX mapping analyses were performed on cubic morphology (Fig. 4A-1, B-1, and C-1) and spine shaped (Fig. 4A-2, B-2, and C-2) crystals from samples Zeo-4A-MK-5, Zeo-4A-MK-20, and Zeo-4A-MK-40, respectively. The Si/Al atomic ratios obtained were 1.071, 1.034, and 1.020 for the cubic crystals, and 1.009, 0.923, and 0.880 for the spine shaped crystals from Zeo-4A-MK-5, Zeo-4A-MK-20, and Zeo-4A-MK-40, respectively. The cubic crystals had higher Si/Al atomic ratios close to unity, indicating the presence of LTA-type zeolite crystals. However, the spine shaped crystals had lower Si/Al ratios, indicating incomplete zeolite formation. The mixture of crystals obtained demonstrates the impact of the heating rate on crystal shape. These results show the suitability of the metakaolin achieved at the low heating rate for the synthesis of zeolite 4A.

### 4.3. FT-IR and Raman analysis of Zeo-4A-MK-$x$ samples achieved from the metakaolin samples MK-(5), MK-(20) and MK-(40)

Fig. 5a displays the elongation and vibration absorption bands of the chemical functions present in the synthetized zeolite samples Zeo-4A-MK-5, Zeo-4A-MK-20 and Zeo-4A-MK-40. The bands appearing in the region 350–490 cm$^{-1}$ and 505–690 cm$^{-1}$ are attributed to the vibration modes of the Si–O bonds and Si–O–Si units, and the stretching modes of the T–O–T units

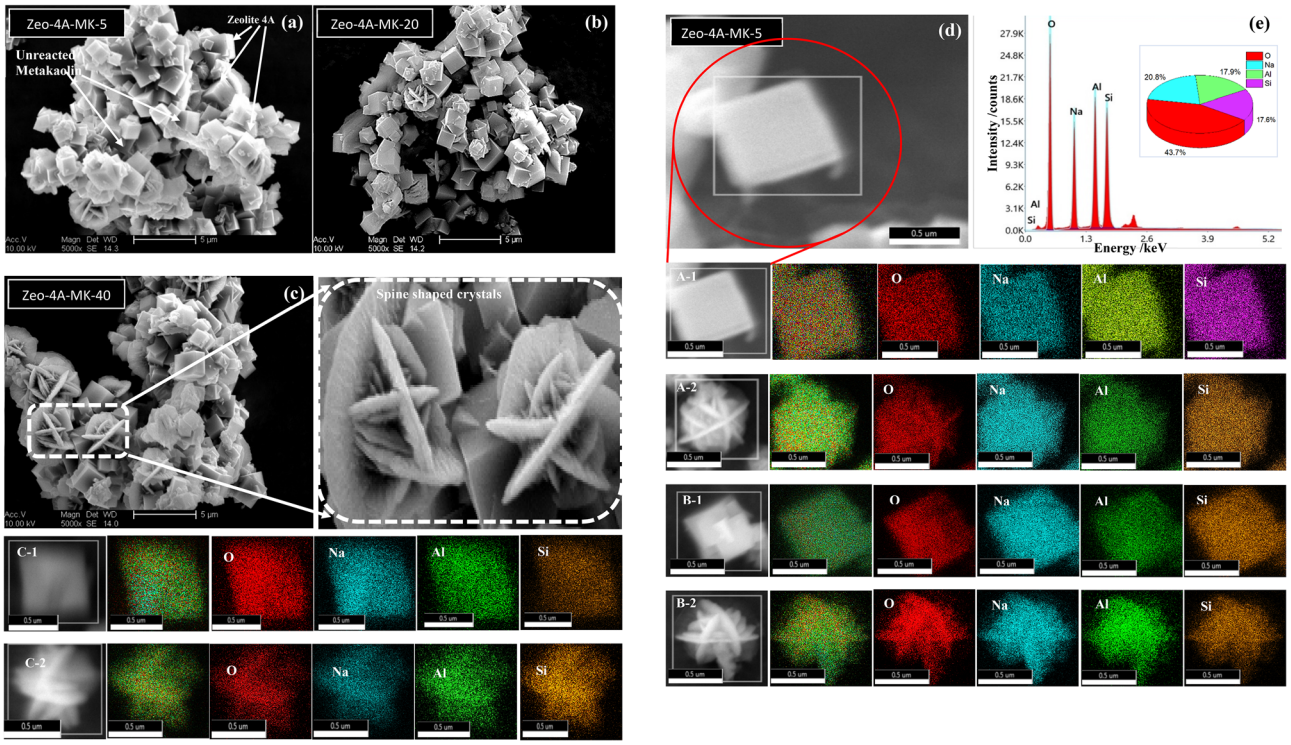


Fig. 4 SEM images of Zeo-4A-MK-*x* materials with *x* = 5 (a), 20 (b) and 40 (c). SEM image (d) and EDX spectra (e) of a single crystal selected from the Zeo-4A-MK-5 sample. EDX-mapping of cubic (A-1, B-1 and C-1), and spine shaped (A-2, B-2 and C-2) crystals of Zeo-4A-MK-5, Zeo-4A-MK-20, and Zeo-4A-MK-40, respectively.

(T = Si or Al). The bands appearing in the range from 905–1000 $cm^{-1}$ are characteristic for the symmetric stretching modes of the Si–O–Al and the Al–OH units. The vibrational modes of the Si–O and Al–O tetrahedral elements are represented by the bands at 655 $cm^{-1}$ and 963 $cm^{-1}$.[47] In addition, the stretching and bending bands of the 4-rings present in the D4R unit of zeolite A and in the 4-ring of the sodalite cage appeared around 464 $cm^{-1}$.[48,49] Moreover, the bands around 3328 $cm^{-1}$ and 1650 $cm^{-1}$ are assigned to asymmetric stretching of Si–OH units and vibrations of Si–O units, respectively.[50] Also, it is noticeable that the spectra of all samples are rather similar and dominated by the bands of zeolite A. Somderam *et al.*, 2019, also found the mentioned bands for the same structural groups present in zeolites, which are structurally similar to those synthetized in this work. Our results suggest that zeolite type 4A was successfully synthesized, while exhibiting variations in absorbance intensities due to incomplete dehydroxylation of kaolin resulting in sodalite and quartz as impurities in the zeolite samples.

Fig. 5b presents the Raman spectra of the Zeo-4A-MK-5, Zeo-4A-MK-20 and Zeo-4A-MK-40 zeolite samples in the spectral range of 50–1000 $cm^{-1}$. The obtained spectra are characteristic

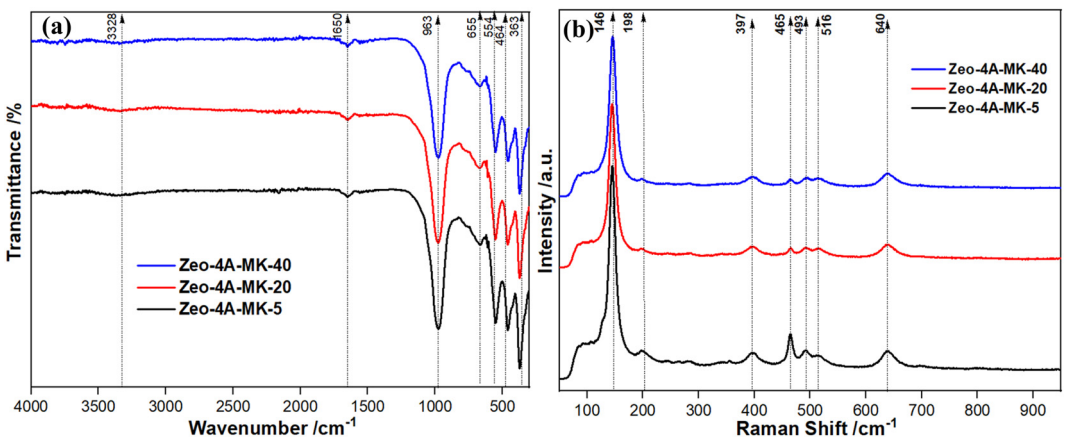


Fig. 5 FT-IR (a) and Raman spectra (b) of synthesized zeolite samples Zeo-4A-MK-5, Zeo-4A-MK-20 and Zeo-4A-MK-40.

of zeolite type 4A with $TO_4$ rings of eight, six and four members with high resolution bands appearing at wavelengths in the ranges 120–200 $cm^{-1}$, 310–400 $cm^{-1}$ and 410–580 $cm^{-1}$, respectively.[51] Furthermore, the bands appearing around 397 $cm^{-1}$ are assigned to the bending modes of Si–O–Si and Al–O–Al rings.[52] The four-membered rings attributable to the Si–O–Al ring are identifiable by the bands appearing around 450–560 $cm^{-1}$.[53] The strong background fluorescence of the T–O (T = Si or Al) bands is observable as the broad band at 146 $cm^{-1}$ corresponding to the 8-membered rings.[29] All absorption bands highlight the formation of zeolite 4A materials. Nevertheless, it should be noted that the samples Zeo-4A-MK-20 and Zeo-4A-MK-40 present some shifts of intensities. These effects might be due to the presence of sodalite and quartz, resulting from the partial conversion of sodium silicate and sodium aluminum silicate in kaolin into the amorphous phase of the metakaolin. Furthermore, a band appearing around 640 $cm^{-1}$ indicates the symmetrical Si–O and Al–O stretching. It is well known that zeolite type 4A having D4R units can be assigned to a band above 600 $cm^{-1}$.[54]

### 4.4. $^{27}$Al and $^{29}$Si Magic Angle Spinning Nuclear Magnetic Resonance spectra (MAS-NMR) of Zeo-4A-MK-*x* samples achieved from the metakaolin samples MK-(5), MK-(20) and MK-(40)

Fig. 6 shows the MAS-NMR $^{29}$Si and $^{27}$Al spectra of the synthesized zeolite samples Zeo-4A-MK-5, Zeo-4A-MK-20 and Zeo-4A-MK-40. The single resonance band of the $^{29}$Si NMR at around -88.89 ppm (Fig. 6a) and the single resonance band of the $^{27}$Al NMR at around 58.09 ppm (Fig. 6b) are shown. Wang *et al.*, 2015, reported the presence of a band around −92.02 ppm for $^{29}$Si and 57.81 ppm for $^{27}$Al for zeolite4A. These values are close to those presented in Fig. 6. The presence of these bands shows that 4 and 6-membered $TO_4$ rings were formed.[22,55] Al–$O_x$ species formed upon metakaolin dissolution migrated to Si–O units to enhance the formation of silica and alumina oligomers. Nevertheless, the samples Zeo-4A-MK-20 and Zeo-4A-MK-40 showed a slight chemical shift, which is more visible in the $^{27}$Al spectrum than in the $^{13}$Si spectrum. This could be explained by the presence of quartz in the synthetized samples. Moreover, the crystalline and ordered structure of the kaolinite did not have enough time to release all its hydroxyl groups. This means that the metakaolin formed at high heating rates occurred with lower reactivity and which can change the coordination of aluminum by oxygen. The reactivity of metakaolin is improved if aluminum has a coordination number in the range from Al(IV) to Al(VI), indicating the presence of fivefold coordinated Al.[56]

### 4.5. $N_2$ adsorption/desorption isotherms of Zeo-4A-MK-*x* samples achieved from the metakaolin samples MK-(5), MK-(20) and MK-(40)

The $N_2$ adsorption–desorption isotherms and pore size distributions of the synthesized zeolite materials Zeo-4A-MK-5, Zeo-4A-MK-20 and Zeo-4A-MK-40 are shown in Fig. 7(a) and (b). All the samples show similar isotherms, which are comparable to that of standard zeolite 4A[38] and represent type IV isotherms according to the IUPAC classification.[57] Fig. 7a shows a hysteresis loop, indicating the presence of textural mesopores and micropore in the samples.[9] This highlights the formation of the zeolite type 4A. The specific surface area, micropore area, pore volume and micropore volume of all samples are summarized in Table S1. The specific surface area of all samples are very close to those in the literature for the similar type of materials.[58,59] The partial conversion of the kaolin during the thermal treatment is probably the reason why the zeolite samples prepared with metakaolin at a high heating rate have more mesopores, which are comparable to those of the zeolite prepared with MK-(5). From Fig. 7b, it is observable that the pore size distributions following the Barrett–Joyner–Halenda (BJH) model are similar for all samples, with a maximum pore diameter of around 10.5 nm. The pore size distribution was also measured using an Autopore 5 mercury intrusion porosimeter (Micromeritics, USA). The results obtained are shown in Fig. S5, which shows the presence of micropores with a maximum diameter of between 11–15 μm in the zeolite samples. The maximum micropores observed in the samples

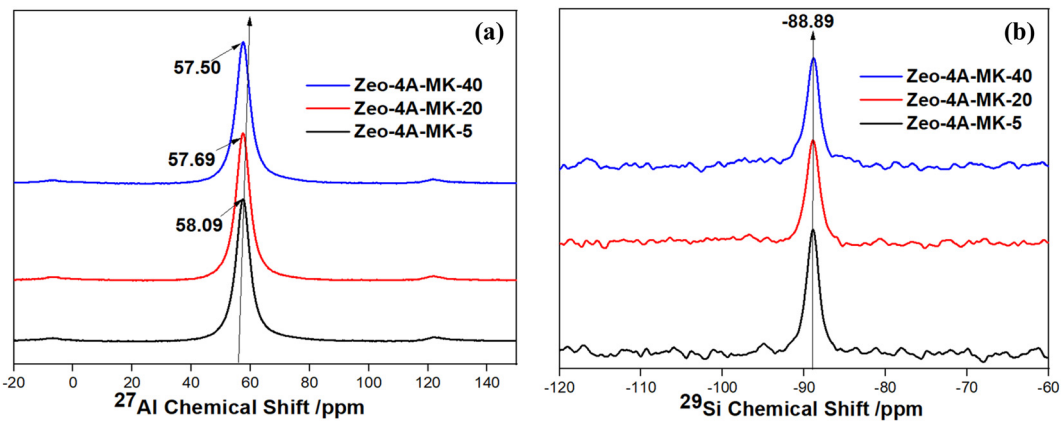


Fig. 6 MAS-NMR spectra $^{29}$Si (a) and $^{27}$Al (b) of Zeo-4A-MK-5, Zeo-4A-MK-20 and Zeo-4A-MK-40.

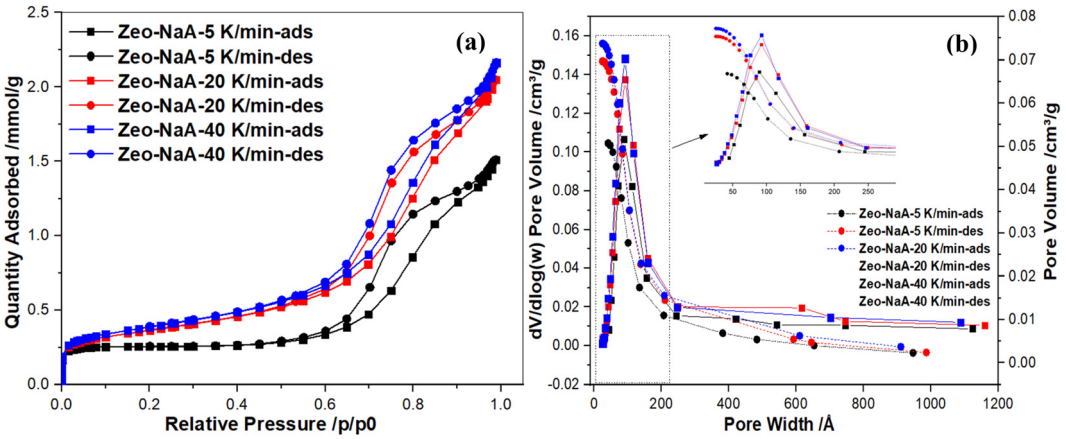


Fig. 7 $N_2$ adsorption/desorption isotherms (a) and BJH pore size distributions (b) including d*V*/dlog (square shape) and pore volume (circle shape) of Zeo-4A-MK-5, Zeo-4A-MK-20 and Zeo-4A-MK-40.

are in the following order: Zeo-4A-MK-40 > Zeo-4A-MK-20 > Zeo-4A-MK-5, which corresponds to the BET results obtained.

## 5. Water vapor adsorption

Fig. 8 shows the water vapor adsorption isotherm curves for Zeo-4A-MK-5, Zeo-4A-MK-20 and Zeo-4A-MK-40 at 25 °C, under a relative humidity of 0–98%. The isotherms obtained are of the type H3,[6] characteristic of adsorption on mesoporous adsorbents,[60] showing increasing amounts of water vapor adsorbed from Zeo-4A-MK-5, followed by Zeo-4A-MK-20 and Zeo-4A-MK-40 derived from MK-(5), MK-(20) and MK-(40) metakaolin samples; water vapor adsorption on zeolite samples increases progressively with the increase of the relative humidity. However, each adsorption curve shows three concavities, the first one for humidity between 0–0.1 characterizing the filling of the mesopore where adsorption takes place, followed by the adsorption on the micropore and mesopore with humidity between 01–0.5; and the third concavity for relative humidity above 0.7, where adsorption with capillary condensation occurs.[61] Maximum adsorption capacities of 9.1, 14.6 and 15.3 mg $g^{-1}$ were obtained for zeolites derived from metakaolin samples MK-(5), MK-(20) and MK-(40), respectively, at the highest moisture value of 98%. Adsorption capacity was highest for zeolite Zeo-4A-MK-40, showing a difference of around 6 mg $g^{-1}$ compared with zeolite Zeo-4A-MK-5. The high adsorption capacity of zeolites Zeo-4A-MK-20 and Zeo-4A-MK-40 could be explained by the large opening pore size of these two samples, as shown by the associated BET analyses, and by the possibility of localization of $Na^+$ ions on the zeolite surface, in the sodalite cages of sites I and I' and in the supercages of sites II. XRD analyses of zeolites derived from metakaolin obtained at high heating rates showed the presence of sodalite and quartz as an additional phase in the zeolite. Sodalites and quartz are additional sources of $Na^+$ ions in the final zeolite product; these observations show that $Na^+$ ions are preferentially localized on the body of the zeolite structure and are easily accessible to water molecules. The possibility of hydrogen bonding between hydrogen atoms in water molecules and oxygen atoms in zeolite cavities is more likely, due to the high charge density of $Na^+$ ions.[62] Previous work shows that $Na^+$ ions localized at the

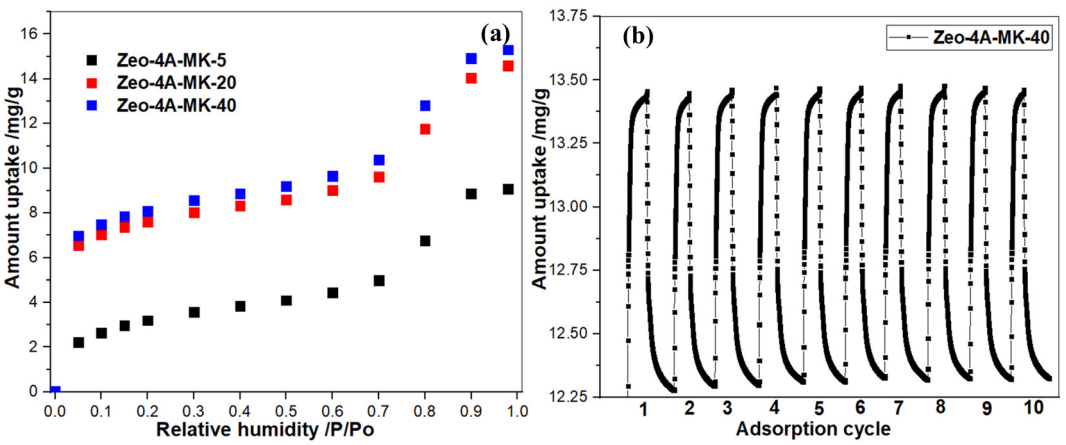


Fig. 8 Experimental water vapor adsorption on Zeo-4A-MK-5, Zeo-4A-MK-20 and Zeo-4A-MK-40 (a), cyclic water vapor adsorption–desorption capacity for Zeo-4A-MK-40 at 20 °C (b).

Table 1 Summary of adsorption capacity of water vapor using different materials

| Silica gel | BET surface[a] | Total pore volume[b] | Method | Pressure, RH[c] (%) | Temp.[d] (°C) | Water vapor uptake | Ref.[h] |
|---|---|---|---|---|---|---|---|
| A++ | 864 | 0.476 | Volumetric | 0.938 kPa | 30 | 0.42[e] | 4 |
| A5BW | 769 | 0.446 | Volumetric | 0.945 kPa | 30 | 0.36[e] | 4 |
| NS10 | 586 | 0.375 | Volumetric | 0.973 kPa | 30 | 0.37[e] | 4 |
| RD2560 | 636 | 0.314 | Volumetric | 0.938 kPa | 30 | 0.31[e] | 4 |
| Zeolite | | | | | | | |
| Zeolite 13X | 772.19 | 0.16 | Gravimetric | 0.98[c] | 25 | 12.11[f] | 69 |
| ZeO–Na–X | 765 | 0.39 | Gravimetric | 0.98[c] | 25 | 12[f] | 70 |
| ZeO–K–X | 211 | 0.11 | Gravimetric | 0.98[c] | 25 | 7[f] | 70 |
| ZeO–Ca–X | 433 | 0.23 | Gravimetric | 0.98[c] | 25 | 14.3[f] | 70 |
| ZeO–Mg–X | 482 | 0.25 | Gravimetric | 0.98[c] | 25 | 17[f] | 70 |
| MgA-1 | 577 | 0.22 | Volumetric | 1 mbar | 25 | 14.7[g] | 8 |
| NaX-0 | 738 | 0.27 | Volumetric | 1 mbar | 25 | 14.01[g] | 8 |
| LiX-1 | 877 | 0.33 | Volumetric | 1 mbar | 25 | 16.4[g] | 8 |
| Zeolite 3A | 660 | — | Volumetric | 0.95 kPa | 25 | 10.25[g] | 71 |
| Zeolite 13X | 743 | 0.3964 | Volumetric | 0.95 kPa | 25 | 15.45[g] | 71 |
| DAY | 704 | 0.268 | Volumetric | 0.95 kPa | 25 | 0.56[g] | 71 |
| Zeolite 3A | N/A | N/A | Volumetric | 1 bar | 25 | 9.37[g] | 64 |
| Zeolite 4A | N/A | N/A | Volumetric | 1 bar | 25 | 11.28[g] | 64 |
| Zeo-4A-MK-5 | 29 | 0.0073 | Gravimetric | 0.98[c] | 20 | 9.1[f] | This work |
| Zeo-4A-MK-20 | 30 | 0.0074 | Gravimetric | 0.98[c] | 20 | 14.6[f] | This work |
| Zeo-4A-MK-40 | 32 | 0.0076 | Gravimetric | 0.98[c] | 20 | 15.[f] | This work |

DAY: dealuminated Y zeolite, N/A: not applicable. [a] $m^2\ g^{-1}$. [b] $cm^3\ g^{-1}$. [c] RH: relative humidity. [d] Temp.: temperature. [e] $g\ g^{-1}$. [f] $mg\ g^{-1}$. [g] $mol\ kg^{-1}$. [h] Ref: reference.

zeolite surface are generally the most accessible to water molecules, which may be due to the kinetics of physisorbed water molecules in the mesopores of Zeo-4A-MK-20 and Zeo-4A-MK-40 zeolites.[63] The low quantity adsorbed for Zeo-4A-MK-5 can be explained by the low content of Lewis base sites generated by the non-framework ions and oxygen atoms of the tetrahedral and octahedral channels present in the zeolite frameworks. However, the quantities adsorbed are relatively higher than those reported by Grace Davison (0.2, 0.18 and 0.17 $mg\ g^{-1}$) and Wang 2020 (1.3 $mmol\ g^{-1}$ and 1.4 $mmol\ g^{-1}$) on zeolites 3A and 4A[64] as well as those of, Kyung-Min Kim *et al.* 2016[6] who presented an adsorption capacity of 1.1 $mmol\ g^{-1}$ with zeolite 4A pellets granulated at a pressure of 1 bar at 25 °C.[65] The difference in adsorption capacity may be linked to the presence of binders in granulated zeolite 4A; these binders block the zeolite pores and slow down the migration of water molecules towards the oxygen's of the zeolite frameworks and the zeolite nuclei. Table 1 summarizes the adsorption capacities of water vapors using zeolites synthesized in this work and other materials. Zeo-4A-MK-40 exhibited high cyclic adsorption–desorption performance that remained virtually constant throughout 10 cycles at 20 °C and 95% humidity, as demonstrated by cyclability studies (see Fig. 8b). These results suggest that Zeo-4A-MK-40 zeolite could be used in high-pressure and pressure swing adsorption applications.

### 5.1. Water vapor isotherms modeling

Experimental water vapor adsorption data were fitted using OriginTM software with Langmuir, Freundlich, Sips and Guggenheim–Anderson–de Boer (GAB) nonlinear isotherm models, to elucidate adsorbent-adsorbate interactions. Fig. 9(a)–(c) show the non-linear fitting isotherms for all Zeo-4A-MK-5, Zeo-4A-MK-20 and Zeo-4A-MK-40 samples. For all zeolite samples, the Langmuir eqn (S2) and Freundlich eqn (S3) models were found unsuitable to predict the equilibrium adsorbed quantities, with both models showing low correlation coefficients ($R^2$) over the entire corresponding relative pressure range where monolayer and multilayer adsorption take place. The Langmuir model shows a process of continuous surface pore coverage as a function of adsorption enthalpy and surface heterogeneity.[66] Furthermore, the Freundlich isotherm, based on the assumption that adsorption energy at the adsorbent surface decreases reciprocally with decreasing adsorption sites, implies infinite multilayer adsorption on heterogeneous surfaces.[66] Furthermore, the Langmuir model provides the highest equilibrium adsorption capacity, comparable to the Freundlich model, suggesting the presence of multilayer adsorption on zeolite surfaces.

The Sips model eqn (S4)[67] is a combination of the Langmuir and Freundlich models, which assumes that the adsorbate surface coverage trends from the most to least active sites, with surface energy heterogeneity. The parameters derived from the Sips model in Table S2 show that the Sips model exhibits a high adsorption capacity at equilibrium, but with low correlation coefficients for all zeolite samples, which characterizes monolayer and pressure-based adsorption as the predominant mechanism on the zeolite surface. The non-correlation of the Sips model could be due to the non-heterogeneity of the adsorbate surface at high relative adsorption humidities.[4]

The GAB isotherm model, eqn (S5), is based on the modification of Brunauer–Emmett–Teller and Langmuir theories, and takes into account both monolayer and multilayer adsorption theory. The GAB model has the advantage of being applicable to a wide range of relative humidity pressures.[68] Table S2, presents the parameters derived from the GAB model, showing close agreement between experimental and model data, the GAB model showed a more accurate correlation than the

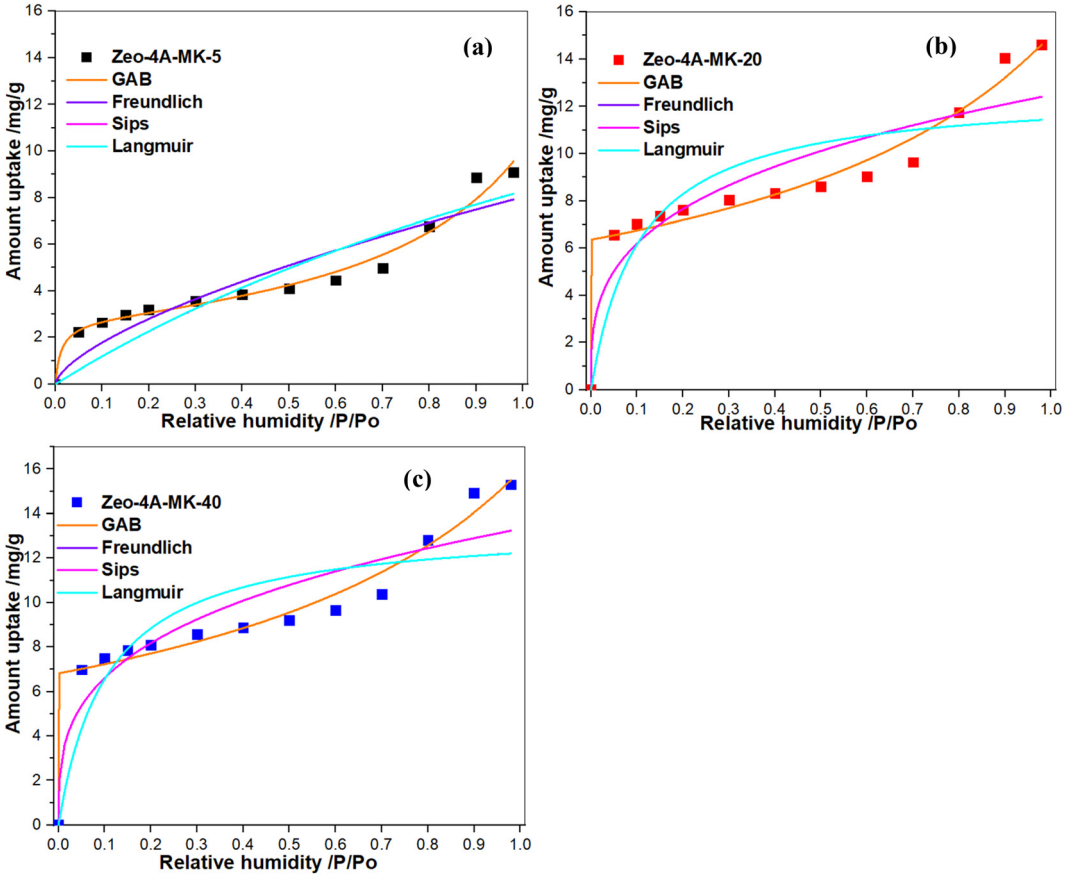


Fig. 9 Langmuir, Freundlich, Sips and GAB fitting to experimental water vapor adsorption data of Zeo-4A-MK-5 (a), Zeo-4A-MK-20 (b) and Zeo-4A-MK-40 (c).

conventional Langmuir, Freundlich and Sips models. The GAB model proved more pronounced, as shown by the $R^2$ values of 0.979, 0.982 and 0.983 obtained for Zeo-4A-MK-5, Zeo-4A-MK-20 and Zeo-4A-MK-40, respectively; the GAB model proved suitable as an equilibrium adsorption capacity prediction model for type H3 isotherms and variable pressures. The good correlation between experimental and modelled data implies that, during the adsorption, there is micropore filling followed by monolayer and multilayer adsorption and the capillary condensation,[4] due to the interactions between water molecules and oxygen atoms in Lewis site zeolite frameworks with energetic heterogeneity.

## 6. Conclusions

The thermal conversion of cameroonian kaolin to metakaolin was performed at different heating rates (5, 20 and 40 K $min^{-1}$). It was observed that the thermal conversion of kaolin to metakaolin occurred in two steps namely a pre-dehydroxylation step (dehydration). The obtained metakaolin samples MK-(5), MK-(20) and MK-(40) were used for the synthesis of zeolite 4A samples, namely Zeo-4A-MK-5, Zeo-4A-MK-20 and Zeo-4A-MK-40. XRD analyses showed that zeolite 4A was successfully synthesized, with minor impurities of sodalite and quartz, due to the partial dehydroxylation of kaolin and incomplete conversion of aluminum silicates and sodium silicate during the zeolitization step.

The amount of the impurities is concomitantly increasing with the heating rate of the thermal kaolin to metakaolin transformation procedure. The incomplete conversion is also visible in the SEM pictures showing an increasing amount of spine-shaped structures from MK-(5) to MK-(40). SEM analysis additionally confirmed the presence of zeolite 4A as uniformly cubic shaped crystals together with unreacted lamellar metakaolin. The synthesized zeolite 4A in the obtained samples exhibited a relative crystallinity of 85.50, 83.18 and 81.01% for Zeo-4A-MK-5, Zeo-4A-MK-20 and Zeo-4A-MK-40 compared to our standard fully crystalline zeolite 4A sample. $N_2$ adsorption–desorption isotherms showed hysteresis loops, indicating the presence of textural mesopores. The specific surface areas calculated using the BET model were 23, 29 and 31 $m^2\ g^{-1}$ for Zeo-4A-MK-5, Zeo-4A-MK-20 and Zeo-4A-MK-40, which is in the typical range for zeolite A.

The water vapor adsorption capacity on synthetic zeolite was in the sequence: Zeo-4A-MK-40 > Zeo-4A-MK-20 > Zeo-4A-MK-5, with a maximum adsorption capacity of 15.3, 14.6 and 9.1 mg $g^{-1}$, respectively. Our study approves the suitability of cameroonian kaolin for the successful synthesis of zeolite 4A for water vapor sorption.

## Author contributions

Cyrille Ghislain Fotsop: writing – original draft, visualization, validation, resources, methodology, investigation, formal analysis, data curation, conceptualization. Alexandra Lieb: validation, supervision, investigation, formal analysis, data curation, writing – review & editing. Franziska Scheffler: validation, supervision, resources, funding acquisition, project administration.

## Conflicts of interest

The authors declare no conflict of interest.

## Data availability

Data available on request.

Supplementary information (SI) is available. See DOI: https://doi.org/10.1039/d5ma00678c.

## Acknowledgements

The authors thank the German Academic Exchange Service (DAAD) and the Graduate Scholarship Program of Saxony-Anhalt for funding. Additionally, the researchers acknowledge their gratitude to Dr-Ing. Markus Wilke and MSc Karsten Harnisch for the assistance with the scanning electron microscope measurements, Ms Marlies Kupfernagel for her help with the TGA measurements and MSc Elias Kluth for his help with the Raman spectroscopy. The researchers also acknowledge their gratitude to the assistance of Ms Sabine Schlüsselburg for DVS measurements.

## References

1 A. Al Ezzi and H. Ma, *Equilibrium Adsorption Isotherm Mechanism of Water Vapor on Zeolites 3A, 4A, X, and Y, in Volume 6: Energy*, American Society of Mechanical Engineers, Tampa, Florida, USA, 2017, V006T08A059, DOI: 10.1115/IMECE2017-72601.

2 G. Goodarzia, S. Dehghani, A. Akbarzadeh and A. Date, Energy Saving Opportunities in air Drying Process in High-pressure Compressors, *Energy Proc.*, 2017, **110**, 428–433, DOI: 10.1016/j.egypro.2017.03.164.

3 C. Du and H. Yang, Synthesis and characterization of zeolite 4A-type desiccant from kaolin, *Am. Mineral.*, 2010, **95**(5–6), 741–746, DOI: 10.2138/am.2010.3288.

4 S.-Y. Woo, H.-S. Lee, H. Ji and Y.-D. Kim, Adsorption Isotherm Model for Analyzing the Adsorption Characteristics of Water Vapor to Commercially Available Silica Gel Adsorbents for Adsorption Desalination Applications, *J. Chem. Eng. Data*, 2021, **66**(2), 1144–1156, DOI: 10.1021/acs.jced.0c00927.

5 A. J. Rieth, S. Yang, E. N. Wang and M. Dincă, Record Atmospheric Fresh Water Capture and Heat Transfer with a Material Operating at the Water Uptake Reversibility Limit, *ACS Cent. Sci.*, 2017, **3**(6), 668–672, DOI: 10.1021/acscentsci.7b00186.

6 K.-M. Kim, H.-T. Oh, S.-J. Lim, K. Ho, Y. Park and C.-H. Lee, Adsorption Equilibria of Water Vapor on Zeolite 3A, Zeolite 13X, and Dealuminated Y Zeolite, *J. Chem. Eng. Data*, 2016, **61**(4), 1547–1554, DOI: 10.1021/acs.jced.5b00927.

7 W. Lim, C. Lee and S. Hamm, Synthesis and characteristics of Na-A zeolite from natural kaolin in Korea, *Mater. Chem. Phys.*, 2021, **261**, 124230, DOI: 10.1016/j.matchemphys.2021.124230.

8 Z. Tahraoui, H. Nouali, C. Marichal, P. Forler, J. Klein and T. J. Daou, Influence of the Compensating Cation Nature on the Water Adsorption Properties of Zeolites, *Molecules*, 2020, **25**(4), 944, DOI: 10.3390/molecules25040944.

9 P. Wang, Q. Sun, Y. Zhang and J. Cao, Synthesis of zeolite 4A from kaolin and its adsorption equilibrium of carbon dioxide, *Materials*, 2019, **12**(9), 1–12, DOI: 10.3390/ma12091536.

10 D. Verboekend, Introducing mesoporosity in zeolite 4A bodies for Rapid CO 2 capture.

11 C. Belviso, *et al.*, Synthesis of magnetic zeolite at low temperature using a waste material mixture: Fly ash and red mud, *Microporous Mesoporous Mater.*, 2015, **202**, 208–216, DOI: 10.1016/j.micromeso.2014.09.059.

12 A. A. B. Maia, R. S. Angélica and R. F. Neves, Use of industrial kaolin waste from the Brazilian Amazon region for synthesis of zeolite A, *Clay Miner.*, 2011, **46**(1), 127–136, DOI: 10.1180/claymin.2011.046.1.127.

13 R. T. Rigo, S. B. C. Pergher, D. I. Petkowicz and J. H. Z. D. Santos, Um novo procedimento de síntese da zeólita A empregando argilas naturais, *Quím. Nova*, 2009, **32**(1), 21–25, DOI: 10.1590/S0100-40422009000100004.

14 A. G. San Cristóbal, R. Castelló, M. A. Martín Luengo and C. Vizcayno, Zeolites prepared from calcined and mechanically modified kaolinsA comparative study, *Appl. Clay Sci.*, 2010, **49**(3), 239–246, DOI: 10.1016/j.clay.2010.05.012.

15 L. Ayele, J. Pérez-Pariente, Y. Chebude and I. Díaz, Conventional versus alkali fusion synthesis of zeolite A from low grade kaolin, *Appl. Clay Sci.*, 2016, (132–133), 485–490, DOI: 10.1016/j.clay.2016.07.019.

16 M. Alkan, Ç. Hopa, Z. Yilmaz and H. Güler, The effect of alkali concentration and solid/liquid ratio on the hydrothermal synthesis of zeolite NaA from natural kaolinite, *Microporous Mesoporous Mater.*, 2005, **86**(1–3), 176–184, DOI: 10.1016/j.micromeso.2005.07.008.

17 P. E. A. Lima, R. S. Angélica and R. F. Neves, Applied Clay Science Dissolution kinetics of metakaolin in sulfuric acid: Comparison between heterogeneous and homogeneous reaction methods, *Appl. Clay Sci.*, 2014, **88–89**, 159–162, DOI: 10.1016/j.clay.2013.12.009.

18 M. Irfan Khan, *et al.*, The pyrolysis kinetics of the conversion of Malaysian kaolin to metakaolin, *Appl. Clay Sci.*, 2017, **146**, 152–161, DOI: 10.1016/j.clay.2017.05.017.

19 K. L. Konan, C. Peyratout, A. Smith, J. Bonnet, S. Rossignol and S. Oyetola, Journal of Colloid and Interface Science Comparison of surface properties between kaolin and

metakaolin in concentrated lime solutions, *J. Colloid Interface Sci.*, 2009, **339**(1), 103–109, DOI: 10.1016/j.jcis.2009.07.019.

20 P. Zemenová, A. Kloužková, M. Kohoutková and R. Král, Investigation of the first and second dehydroxylation of kaolinite, *J. Thermal Anal. Calorim.*, 2014, 633–639, DOI: 10.1007/s10973-014-3748-9.

21 H. Wang, C. Li and Z. Peng, Characterization and thermal behavior of kaolin, *J. Therm. Anal. Calorim.*, 2011, 157–160, DOI: 10.1007/s10973-011-1385-0.

22 J. Sanz and M. Serratosa, **Si and *'AI NMR Study of Zeolite Formation from Alkali-Leached Kaolinites, *J. Phys. Chem.*, 1990, **94**(2), 760–765.

23 I. Majchrzak-Kucęba and W. Nowak, A thermogravimetric study of the adsorption of CO2 on zeolites synthesized from fly ash, *Thermochim. Acta*, 2005, **437**(1–2), 67–74, DOI: 10.1016/j.tca.2005.06.003.

24 Z. Zhou, G. Jin, H. Liu, J. Wu and J. Mei, Applied Clay Science Crystallization mechanism of zeolite A from coal kaolin using a two-step method, *Appl. Clay Sci.*, 2014, (97–98), 110–114, DOI: 10.1016/j.clay.2014.05.015.

25 C. G. Fotsop, A. Lieb and F. Scheffler, Elucidation of the thermo-kinetics of the thermal decomposition of cameroonian kaolin: mechanism, thermodynamic study and identification of its by-products, *RSC Adv.*, 2025, **15**(39), 32172–32187, DOI: 10.1039/d5ra05149e.

26 A. Souri, F. Golestani-fard, R. Naghizadeh and S. Veiseh, Applied Clay Science An investigation on pozzolanic activity of Iranian kaolins obtained by thermal treatment, *Appl. Clay Sci.*, 2015, **103**, 34–39, DOI: 10.1016/j.clay.2014.11.001.

27 H. E. Mgbemere, G. I. Lawal, I. C. Ekpe and A. L. Chaudhary, Synthesis of zeolite-A using kaolin samples from Darazo, Bauchi state and Ajebo, Ogun state in Nigeria, *Nigerian J. Technol.*, 2018, **37**(1), 87, DOI: 10.4314/njt.v37i1.12.

28 H. E. Mgbemere, *et al.*, Synthesis of zeolite-a using kaolin samples from darazo, bauchi state and ajebo, ogun state in nigeria, *Niger. J. Technol*, 2018, **37**(1), 87–95.

29 W. Wang, Q. Feng, K. Liu, G. Zhang, J. Liu and Y. Huang, A novel magnetic 4A zeolite adsorbent synthesised from kaolinite type pyrite cinder (KTPC), *Solid State Sci.*, 2015, **39**, 52–58, DOI: 10.1016/j.solidstatesciences.2014.11.012.

30 K. Brylewska, P. Rożek, M. Król and W. Mozgawa, The influence of dealumination/desilication on structural properties of metakaolin-based geopolymers, *Ceram. Int.*, 2018, **44**(11), 12853–12861, DOI: 10.1016/j.ceramint.2018.04.095.

31 Q. Wan, *et al.*, Geopolymerization reaction, microstructure and simulation of metakaolin-based geopolymers at extended Si/Al ratios, *Cement Concrete Comp.*, 2017, **79**, 45–52, DOI: 10.1016/j.cemconcomp.2017.01.014.

32 P. Ptáček, D. Kubátová, J. Havlica, J. Brandštetr, F. Šoukal and T. Opravil, Isothermal kinetic analysis of the thermal decomposition of kaolinite: The thermogravimetric study, *Thermochim. Acta*, 2010, **501**(1–2), 24–29, DOI: 10.1016/j.tca.2009.12.018.

33 P. Ptáček, F. Frajkorová, F. Šoukal and T. Opravil, Kinetics and mechanism of three stages of thermal transformation of kaolinite to metakaolinite, *Powder Technol.*, 2014, **264**, 439–445, DOI: 10.1016/j.powtec.2014.05.047.

34 R. U. N. Foko, C. G. Fotsop, D. R. T. Tchuifon, C. Banenzoué and A. G. B. Azebaze, Green synthesis of magnetic type Zeolites 4A as catalyst for the elimination of quinoline yellow by the Fenton process: Optimization and kinetic investigation, *Hybrid Adv.*, 2025, **9**, 100401, DOI: 10.1016/j.hybadv.2025.100401.

35 F. Franco and L. A. Pérez-maqueda, The influence of ultrasound on the thermal behaviour of a well ordered kaolinite, *Thermochim. Acta*, 2003, **404**, 71–79, DOI: 10.1016/S0040-6031(03)00065-0.

36 F. P. Tchoumi, A. K. Tamo, G. Doungmo, C. G. Fotsop, J. C. Kemmegne-Mbouguen and E. Ngameni, Polymer-free nanocomposite from zeolite and acetylene carbon black as glassy carbon modifier platform for simultaneous electrochemical quantification of acetaminophen and caffeine, *J. Appl. Electrochem.*, 2024, **54**(8), 1901–1918, DOI: 10.1007/s10800-024-02076-1.

37 C. G. Fotsop, A. Lieb and F. Scheffler, Tailoring the water vapor adsorption properties by thermal performance analysis of post-synthetically ion-exchanged LTA zeolite derived from Cameroonian kaolin, *J. Ind. Eng. Chem.*, 2025, DOI: 10.1016/j.jiec.2025.08.017.

38 K. L. T. Nguena, *et al.*, Mathematical modeling approach for the green synthesis of high-performance nanoporous zeolites Na-X optimized for water vapor sorption, *Mater. Today Commun.*, 2023, **37**, 107406, DOI: 10.1016/j.mtcomm.2023.107406.

39 L. Ayele, J. Pérez-Pariente, Y. Chebude and I. Díaz, Conventional versus alkali fusion synthesis of zeolite A from low grade kaolin, *Appl. Clay Sci.*, 2016, (132–133), 485–490, DOI: 10.1016/j.clay.2016.07.019.

40 E. I. Basaldella, A. Kikot and J. C. Tara, Effect of aluminum concentration on crystal size and morphology in the synthesis of a NaAl zeolite, *Mater. Lett.*, 1997, **31**, 83–86.

41 S. Chandrasekhar, P. N. Pramada, C. M. Section and K. State, Investigation on the Synthesis of Zeolite NaX from Kerala Kaolin, *J. Porous Mater.*, 1999, **297**, 283–297.

42 M. I. Khan, K. Azizli, S. Su and Z. Man, Sodium silicate-free geopolymers as coating materials: Effects of Na/Al and water/solid ratios on adhesion strength, *Ceram. Int.*, 2015, **41**, 2794–2805, DOI: 10.1016/j.ceramint.2014.10.099.

43 A. Iqbal, H. Sattar, R. Haider and S. Munir, Synthesis and characterization of pure phase zeolite 4A from coal fly ash, *J. Cleaner Prod.*, 2019, **219**, 258–267, DOI: 10.1016/j.jclepro.2019.02.066.

44 A. R. Loiola, J. C. R. A. Andrade, J. M. Sasaki and L. R. D. Silva, Journal of Colloid and Interface Science Structural analysis of zeolite NaA synthesized by a cost-effective hydrothermal method using kaolin and its use as water softener, *J. Colloid. Interface Sci.*, 2012, **367**(1), 34–39, DOI: 10.1016/j.jcis.2010.11.026.

45 J. K. Kim and H. D. Lee, Journal of Industrial and Engineering Chemistry Effects of step change of heating source on synthesis of zeolite 4A from coal fly ash, *J. Ind. Eng. Chem.*, 2009, **15**, 736–742, DOI: 10.1016/j.jiec.2009.09.055.

46 H. Liu, S. Peng, L. Shu, T. Chen, T. Bao and R. L. Frost, Magnetic zeolite NaA: Synthesis, characterization based on metakaolin and its application for the removal of Cu2 +, Pb2+, *Chemosphere*, 2013, **91**(11), 1539–1546, DOI: 10.1016/j.chemosphere.2012.12.038.

47 Z. Zhou, G. Jin, H. Liu, J. Wu and J. Mei, Crystallization mechanism of zeolite A from coal kaolin using a two-step method, *Appl. Clay Sci.*, 2014, **97–98**, 110–114, DOI: 10.1016/j.clay.2014.05.015.

48 S. Somderam, A. S. Abd, A. H. Abdullah and R. Mat, Characterisation of NaA Zeolite Made from Malaysian Kaolin, *Chem. Eng. Trans.*, 2019, **7**, 325–330, DOI: 10.3303/CET1972055.

49 P. Wang, Q. Sun, Y. Zhang and J. Cao, Synthesis of zeolite 4A from kaolin and its adsorption equilibrium of carbon dioxide, *Materials*, 2019, **12**, 9, DOI: 10.3390/ma12091536.

50 W. Mozgawa, M. Król and K. Barczyk, FT-IR studies of zeolites from different structural groups, *Chemik*, 2011, **65**(7), 671–674.

51 Y. Yu, G. Xiong, C. Li and F.-S. Xiao, Characterization of aluminosilicate zeolites by UV Raman spectroscopy, *Stud. Surf. Sci. Catal.*, 2001, 217.

52 F. H. Kamgang Djioko, C. G. Fotsop, G. Kamgang Youbi, S. C. Nwanonenyi, E. E. Oguzie and C. Ada Madu, Efficient removal of pharmaceutical contaminant in wastewater using low-cost zeolite 4A derived from kaolin: Experimental and theoretical studies, *Mater. Chem. Phys.*, 2024, **315**, 128994, DOI: 10.1016/j.matchemphys.2024.128994.

53 P. Mcmillan, Structural studies of silicate glasses and melts-applications and limitations of Raman spectroscopy, *Am. Mineral.*, 1984, 622–644.

54 P. K. Dutta and B. D. Barco, Raman Spectroscopy of Zeolite A: Influence of SVAI Ratio, *J. Phys. Chem.*, 1988, **2**, 354–357.

55 S. Su, H. Ma and X. Chuan, Hydrothermal synthesis of zeolite A from K-feldspar and its crystallization mechanism, *Adv. Powder Technol.*, 2016, **27**(1), 139–144, DOI: 10.1016/j.apt.2015.11.011.

56 P. Taylor, *et al.*, Separation Science and Technology Zeolite Apgiia for Adsorption Based Carbon Dioxide Capture Zeolite Apgiia for Adsorption Based Carbon Dioxide Capture, *Sep. Sci. Technol.*, 2013, 37–41, DOI: 10.1080/01496395.2012.703751.

57 M. Thommes, *et al.*, Physisorption of gases, with special reference to the evaluation of surface area and pore size distribution (IUPAC Technical Report), *Pure Appl. Chem.*, 2015, **87**, 1051–1069, DOI: 10.1515/pac-2014-1117.

58 W. Feng, Z. Wan, J. Daniels, Z. Li, G. Xiao and J. Yu, Synthesis of high quality zeolites from coal fly ash: Mobility of hazardous elements and environmental applications, *J. Cleaner Prod.*, 2018, **202**(20), 390–400, DOI: 10.1016/j.jclepro.2018.08.140.

59 Z. Wu, *et al.*, Preparation, characterization, and performance of 4A zeolite based on opal waste rock for removal of ammonium ion, *Adsorpt. Sci. Technol.*, 2018, **36**(9–10), 1700–1715, DOI: 10.1177/0263617418803012.

60 D. Panda, E. A. Kumar and S. K. Singh, Amine Modification of Binder-Containing Zeolite 4A Bodies for Post-Combustion CO 2 Capture, *Ind. Eng. Chem. Res.*, 2019, **58**(13), 5301–5313, DOI: 10.1021/acs.iecr.8b03958.

61 J. C. Moïse, J. P. Bellat and A. Méthivier, Adsorption of water vapor on X and Y zeolites exchanged with barium, *Microporous Mesoporous Mater.*, 2001, **43**(1), 91–101, DOI: 10.1016/S1387-1811(00)00352-8.

62 C. Kosanović, B. Subotić and A. Čižmek, Thermal analysis of cation-exchanged zeolites before and after their amorphization by ball milling, *Thermochim. Acta*, 1996, **276**, 91–103, DOI: 10.1016/0040-6031(95)02792-0.

63 F. Benaliouche, N. Hidous, M. Guerza, Y. Zouad and Y. Boucheffa, Characterization and water adsorption properties of Ag- and Zn-exchanged A zeolites, *Microporous Mesoporous Mater.*, 2015, **209**, 184–188, DOI: 10.1016/j.micromeso.2014.10.039.

64 Y. Wang, Measurements and Modeling of Water Adsorption Isotherms of Zeolite Linde-Type A Crystals, *Ind. Eng. Chem. Res.*, 2020, **59**(17), 8304–8314, DOI: 10.1021/acs.iecr.9b06891.

65 M. Llano-Restrepo and M. A. Mosquera, Accurate correlation, thermochemistry, and structural interpretation of equilibrium adsorption isotherms of water vapor in zeolite 3A by means of a generalized statistical thermodynamic adsorption model, *Fluid Phase Equilib.*, 2009, **283**(1–2), 73–88, DOI: 10.1016/j.fluid.2009.06.003.

66 F. Raganati, M. Alfe, V. Gargiulo, R. Chirone and P. Ammendola, PT SC, *Chem. Eng. Res. Des.*, 2018, **134**, 540–552, DOI: 10.1016/j.cherd.2018.04.037.

67 J. Sreńscek-Nazzal, U. Narkiewicz, A. W. Morawski, R. J. Wróbel and B. Michalkiewicz, Comparison of Optimized Isotherm Models and Error Functions for Carbon Dioxide Adsorption on Activated Carbon, *J. Chem. Eng. Data*, 2015, **60**(11), 3148–3158, DOI: 10.1021/acs.jced.5b00294.

68 X. Ma, W. Shen, X. Li, Y. Hu, X. Liu and X. Lu, Experimental investigation on water adsorption and desorption isotherms of the Longmaxi shale in the Sichuan Basin, *China Sci. Rep.*, 2020, **10**(1), 13434, DOI: 10.1038/s41598-020-70222-8.

69 K. L. T. Nguena, *et al.*, Unraveling the sorption mechanism of industrial dyes onto Zr-based MOFs: computational and experimental modelling for highly efficient removal, *Mater. Adv*, 2024, **6**(2), 579–597, DOI: 10.1039/D4MA00818A.

70 F. D. S. Feudjio, *et al.*, Tunable water vapor adsorption properties on ion exchange microporous zeolite Na-X derived from natural kaolin, *Inorg. Chem. Commun.*, 2025, **177**, 114379, DOI: 10.1016/j.inoche.2025.114379.

71 K.-M. Kim, H.-T. Oh, S.-J. Lim, K. Ho, Y. Park and C.-H. Lee, Adsorption Equilibria of Water Vapor on Zeolite 3A, Zeolite 13X, and Dealuminated Y Zeolite, *J. Chem. Eng. Data*, 2016, **61**(4), 1547–1554, DOI: 10.1021/acs.jced.5b00927.